The paucity of supershear earthquakes on large faults governed by rate and state friction

Chao Liang[1,2], Jean-Paul Ampuero[2], and Daniel Pino Muñoz[3]

[1]Institute for Disaster Management and Reconstruction (IDMR), Sichuan University, 610207, Chengdu, China

[2]Géoazur, Université Côte d'Azur (UCA), IRD, CNRS, Observatoire de la Côte d'Azur, 06560, Valbonne, France

[3]Centre de Mise en Forme des Matériaux (CEMEF), Mines-ParisTech, PSL Research University, CNRS UMR 7635, 1 rue Claude Daunesse, 06904, Sophia Antipolis Cedex, France, France

Key Points:

- Supershear rupture is favored in rate-and-state cycle models on long faults in a parameter range that is not common.
- Decreasing a/b or increasing the nucleation length to fault width ratio increases the initial stress of earthquakes and favors supershear ruptures.
- Most supershear events occur at a high background stress ($S < 0.70$) and via a direct supershear transition.

Corresponding author: Chao Liang, `chaovite@gmail.com`

Abstract

Supershear earthquakes are rare compared to their subshear counterparts, but the cause for their paucity remains to be understood. We investigate for the first time the prevalence of supershear ruptures across multiple earthquake cycles on long faults using rate-and-state friction and a 2.5D approximation that accounts for the finite seismogenic width W. We find supershear events occur only in a narrow range of friction parameters that is not commonly observed in laboratory experiments, which may explain its rarity in nature. Particularly, the ratio between direct and evolution effects of rate-and-state friction needs to be low (a/b <0.4) and the nucleation length has to be sufficiently large compared to W, but not too large that it causes a transition from seismic to aseismic slip. Our numerical and analytical developments contribute fundamentally to understanding the state of stress on long faults over multiple earthquake cycles and their potential for hosting supershear earthquakes.

Plain Language Summary

Supershear earthquakes, those that rupture faster than shear wave speed, can generate strong shaking. They occur rarely in nature, but why they are rare has not yet been understood. In this study, we model sequences of earthquakes on a long fault assuming a fault friction motivated by (relatively slow) laboratory experiments. Importantly, our model accounts for the fact that the largest earthquake ruptures are much longer than deep. Our simulations indicate the fault frictional properties and fault width exert important control on the occurrence rate of supershear earthquakes. Particularly, the fault has to be able to accumulate sufficient stress to produce supershear earthquakes. The range of frictional properties that favors supershear ruptures in our model is not commonly observed in laboratory experiments, which may explain why supershear earthquakes are rare in nature.

Introduction

It is now well established that large strike-slip earthquakes can rupture at speeds higher than shear wave speed. This fact has been well proven by seismological observations (Bouchon & Vallée, 2003; Dunham & Archuleta, 2004; Ellsworth et al., 2004; Vallée & Dunham, 2012; Bao et al., 2019) and supported by laboratory experiments (Wu et al., 1972; Rosakis et al., 1999; Xia et al., 2004, 2005; Mello et al., 2014) and theoretical and numerical analysis (Burridge, 1973; Andrews, 1976; Dunham et al., 2003; Dunham, 2007). Due to the generation of shear and Rayleigh wave Mach fronts, supershear ruptures have the potential to carry strong shaking farther away from the fault than sub-Rayleigh ruptures, though this effect could be suppressed by reduced wavefield coherence caused by source or medium heterogeneities (Bizzarri et al., 2010; Vyas et al., 2018). So far, the mechanism that controls the frequency of occurrence of supershear earthquakes is still poorly understood.

Since the discovery of supershear earthquakes in the early 1980s, multiple supershear transition mechanisms have been proposed. The earliest one is the Burridge-Andrews (BA) mechanism (Burridge, 1973; Andrews, 1976; Dunham, 2007), in which a sub-Rayleigh rupture jumps to supershear provided a high enough initial shear stress and a sufficient long propagation distance. Later studies show that favorable stress asperities or barriers (Y. Liu & Lapusta, 2008; Lu et al., 2009; Weng et al., 2015), fault roughness and geometric complexities (Bruhat et al., 2016; Ryan & Oglesby, 2014), fault damage zone (Huang et al., 2016) and free surface effects (Kaneko & Lapusta, 2010; Hu et al., 2019; J. Xu et al., 2021) can also induce supershear rupture. Particularly, given a sufficiently high initial stress, a sub-Rayleigh rupture can accelerates smoothly into a supershear speed via a direct transition mechanism, without experiencing the mother-daughter crack transition of the classic BA mechanism (C. Liu et al., 2014; Kammer et al., 2018).

However, despite these numerous possible mechanisms, supershear earthquakes remain rare. Up to now, only about ten supershear ruptures have been reliably documented (Das, 2015). The rareness of supershear earthquakes could be due to limitations of observation techniques or to earthquake source physics. Indeed, measuring rupture speed is challenging given scarce, frequency-limited data and uncertain earth structure (Meng et al., 2016; Zeng et al., 2020). However, a recent global survey (Bao et al., submitted manuscript) using state-of-the-art teleseismic back-projection rupture imaging (Bao et al., 2019) overcomes the observational bias but still founds merely 15% supershear ruptures among large strike-slip earthquakes since 2000. Here, we show that the rarity of supershear earthquakes could be controlled by fault frictional properties.

Existing modeling of supershear ruptures focuses on simulating a single dynamic earthquake (Dunham, 2007; Bruhat et al., 2016; Gabriel et al., 2012; Huang et al., 2016; Vyas et al., 2018), an approach limited by the arbitrariness of prescribed initial conditions. In those models, the initial stress is found to have a major control on the viability of supershear rupture. Yet the odds of achieving favorable initial conditions cannot be evaluated in such a framework. An approach that can self-consistently simulate spontaneous states of fault stress is earthquake cycle modeling. However, most earthquake cycle models assume either 2D anti-plane shear (Kaneko et al., 2011; Erickson et al., 2017; Miyake & Noda, 2019; Abdelmeguid et al., 2019; Thakur et al., 2020) or the quasi-dynamic approximation (Y. Liu & Rice, 2005; Richards-Dinger & Dieterich, 2012; Luo & Ampuero, 2018; Ozawa & Ando, 2021; Barbot, 2021), thus cannot produce supershear earthquakes. A few 3D fully dynamic earthquake cycle codes for inplane rupture have been developed (Lapusta & Liu, 2009; D. Liu et al., 2020; Noda, 2021) but they are computationally expensive and, to the best of our knowledge, have not been used to investigate the variation of dynamic rupture speeds over multiple earthquake cycles. This work is the first attempt to tackle this challenge. We further account for a finite seismogenic width, W, which has an important control on the rupture dynamics of large earthquakes (Weng & Ampuero, 2019, 2020).

We model fully-dynamic earthquake cycles on a homogeneous elongated fault governed by conventional rate-and-state friction (Dieterich, 1978; Ruina, 1983) with the aging law of state evolution, embedded in a linear elastic material. We use the spectral element method (SEM) for spatial discretization (Kaneko et al., 2011; Seki, 2017). We account for a finite seismogenic width by a 2.5D approoach (Figure S1) that provides an adequate approximation of 3D elongated ruptures while retaining the computational efficiency of 2D models (Lehner et al., 1981; Weng & Ampuero, 2019, 2020). To facilitate distilling fundamental understanding, we keep the model simple, by neglecting complex mechanisms such as dynamic weakening (Rice, 2006; Noda & Lapusta, 2010; Dunham et al., 2011; Noda & Lapusta, 2013; Viesca & Garagash, 2015), fault roughness (Bruhat et al., 2016; Romanet & Ozawa, 2021), heterogeneous frictional properties (Luo & Ampuero, 2018), and off-fault inelastic deformation (Templeton & Rice, 2008; S. Xu et al., 2012). Using fracture mechanics theory, we first derive an approximate expression of the state of stress right before a characteristic earthquake and identify the key dimensionless parameters that control it. While these expressions cannot predict the exact conditions for supershear rupture, they provide a theoretical basis to interpret the results of our numerical simulations. We then conduct a comprehensive parametric study scanning the two key dimensionless parameters, and identify the conditions that favor recurrent supershear ruptures. Finally, we discuss potential relations between our model results and available observations, limitations of our current model and possible future extensions.

Theoretically expected supershear conditions

We model sequences of earthquakes on a velocity-weakening (VW) patch sandwiched between stably creeping segments, featuring a smooth transition along strike to velocity-strengthening friction (VS) and then to a steadily creeping section (see Figure S1). Regardless of the mechanism of supershear transition, a higher initial fault stress always favors supershear rupture. Initial (pre-earthquake) fault shear stress is conventionally quantified by the ratio between strength excess and stress drop, $S = (\tau_p - \tau_0)/(\tau_0 - \tau_r)$. When S is too high, supershear transition is not possible (Burridge, 1973; Andrews, 1976; Dunham, 2007; Hu et al., 2019; Kammer et al., 2018) unless favorable heterogeneity exists (Dunham et al., 2003; Y. Liu & Lapusta, 2008; Weng et al., 2015). Here, we summarize key steps for deriving an expression for the S value right before characteristic earthquakes, using fracture mechanics. A complete derivation is given in the supplementary material.

The coseismic peak (τ_p) and residual stresses (τ_r) in rate-and-state friction are estimated, under basic assumptions, in equations (S.22) and (S.23). Their difference is the strength drop:

$$\tau_p - \tau_r = \sigma_n b \ln\left(\frac{V_{co} T_n}{d_c}\right), \tag{1}$$

where σ_n is the effective normal stress, b the coefficient quantifying the evolution effect of rate-and-state friction, V_{co} the coseismic peak slip rate, T_n the earthquake interevent time, and d_c the characteristic distance of state evolution. The initial stress τ_0 accumulated since the last characteristic earthquake is

$$\tau_0 = \tau_r + \dot{\tau} T_n, \tag{2}$$

where $\dot{\tau}$ is the secular stressing rate on the fault. For elongated faults, $\dot{\tau} = C_s V_{pl} G/W$, where C_s is a geometric factor that modulates the elastic stiffness of the fault ($4/\pi$ for buried faults, $2/\pi$ for shallow surface faults), V_{pl} the secular fault slip rate imposed by plate tectonics, and G the shear modulus. The final task is to estimate the earthquake interevent time T_n. During interseismic periods, aseismic slip areas emerge at the boundaries between VS and VW regions, then expand into the locked VW region, and eventually grow up to the critical nucleation size L_n, leading to earthquake nucleation, as shown in Figure 5 in Cattania and Segall (2019). T_n is controlled by the time needed for this aseismic slip expansion process, which can be estimated using fracture mechanics. At the slowly propagating front of aseismic slip, the fracture toughness implied by rate-and-state friction is negligible (Cattania, 2019) and the fracture mechanics energy balance reduces to a balance between the stress intensity factor due to stress change within the VW creeping patch and the one due to slip in the VS region. Following Cattania (2019) but adapting the stress intensity factors to the 2.5D geometry (supplementary material), we obtain an expression for T_n, equation (S.34). The resulting strength excess before characteristic earthquakes is

$$S = \frac{\tau_p - \tau_r}{\tau_0 - \tau_r} - 1 = \alpha \frac{1}{C_s(1-\nu)\pi} \frac{1}{\eta} \frac{1}{1-a/b} \frac{W}{L_n} - 1, \tag{3}$$

where ν is Poisson's ratio, α a parameter given in equation (S.36), which typically varies between 1.1 to 1.6, and η a monotonically increasing function of L_n/W given in equation (S.31) and plotted in Figure S3.

The two key dimensionless parameters that control S are a/b and W/L_n. Decreasing either a/b or W/L_n decreases S, which should favor the occurrence of supershear earthquakes. Physically speaking, for a fixed value of b, a lower a tends to increase the stress change in the nucleation patch, according to equation (S.31), which in turn increases T_n. At fixed W, increasing L_n increases the interseismic slip needed to drive nucleation, thus implying a longer interseismic period. Both effects lead to a higher initial stress prior to the next earthquake. On the other hand, a small ratio W/L_n is known to suppress seismic rupture (Y. Liu & Rice, 2005; Rubin, 2008), which competes against supershear rupture. In the limit of $a/b \rightarrow 1$, S tends to $+\infty$, which suppresses supershear transition. Therefore, we expect a cut-off a/b value above which supershear earthquakes on (conventional) rate-and-state faults are not possible.

Even though our earthquake cycle simulations do not include the effect of dynamic weakening, we develop an analytical estimate of the S ratio before characteristic earthquakes in the presence of strong velocity-weakening in the supplementary material (Text S4). As a result of the much lower dynamic friction coefficient $f_w \sim 0.1$ (Rice, 2006; Dunham et al., 2011; Gabriel et al., 2012), the limiting effect of a/b on supershear occurrence diminishes and W/L_n remains the key dimensionless parameter.

The estimate of S presented here is only valid in the limit where linear elastic fracture mechanics applies, namely when the process zone size R_0 (see equation (S.4) for rate-and-state) is much smaller than any other length scale of the problem, including W. As we shall see, this assumption is violated in the parameter range where supershear is favored in the current model, and we expect appreciable deviations between the analytically derived S ratios and those obtained in numerical simulations. Nonetheless, the theoretical development here is highly instrumental in interpreting our numerical results.

Numerical results

Guided by the theoretical analysis in the previous section, we systematically study the effect of the controlling parameters a/b and L_n/W using numerical simulations. A detailed list of parameter settings is presented in the supplementary material (Table S1). As the true nucleation length L_n is unknown prior to simulation, we use as proxy the theoretical estimate L_{RA} by Rubin and Ampuero (2005) for 2D plane strain (equation (S.6) in the supplementary material). L_{RA} generally scales with L_n but can differ significantly due to 2.5D effects at large L_n/W or due to departures from the small-scale yielding assumption of linear elastic fracture mechanics at large R_0/W (see Figure S4). To vary a/b, we fix $b = 0.01$ and vary a from 0.1 to 0.7. To use the same mesh for all simulations and guarantee sufficient resolution, we set the average grid spacing to 125 m, R_0 to 1-2 km, fault length L to 40 km, and vary W between 2 and 10 km. In our simulations, the fault aspect ratio L/W varies between 4 and 20.

By varying the frictional parameters, we are able to produce earthquake sequences with a rich spectrum of rupture styles. Figure 1 shows the evolution of different rupture styles when varying L_{RA}/W and fixing a/b at 0.2. As we increase L_{RA}/W, the earthquake sequence transitions from purely sub-Rayleigh (SR) events, to alternating SR and supershear (SS) events, to purely SS events, then to weak partial ruptures, and finally to aseismic slip. At the same time, we observe a consistent decrease of pre-earthquake S ratio. This is remarkably consistent with our theoretical analysis in the previous section. Notably, the alternation of SR and SS events within the same earthquake sequence arises from differences in the stress drops of SR and SS events due to different peak slip rates (see Text S3.2 and Figure S5 for detailed explanation). Due to the healing effect induced by the finite seismogenic width W, dynamic events exhibit pulse-like rupture similar to those in 3D simulations (Dunham & Archuleta, 2004; Weng & Ampuero, 2019). This 3D effect does not exist in 2D but is captured by our 2.5D simulations.

A "phase diagram" that provides a more complete view on how rupture styles depend on both a/b and L_{RA}/W is presented in Figure 2. As shown in Figure 2a, we find a particular range of parameter values, $a/b < 0.4$ and $L_{RA}/W \sim [0.2, 1.2]$, that favors supershear occurrence. Specifically, as a/b increases, the permissible range of L_{RA}/W for supershear events shrinks and when $a/b \geq 0.4$ supershear ruptures are not possible. At larger L_{RA}/W, we observe a transition to weak partial ruptures and eventually aseismic slip, indicated by a lower peak slip rate and higher partial rupture rate in Figures 2d and 2e, caused by the stabilization effect of a narrow fault width (Y. Liu & Rice, 2005). The rate of supershear occurrence can be largely explained by the numerically computed median S ratio, as shown in Figure 2b (all events) and Figure 2c (supershear events), which obeys the same trend as in our analytical derivation: S decreases as a/b decreases or L_{RA}/W increases. The cut-off a/b can be understood by the fact that the supershear transition is not possible when S exceeds a critical value, on faults with homogeneous stress and strength (Dunham, 2007; Kammer et al., 2018). In fact, most of the supershear events obtained here have a median S ratio smaller than 0.7, as shown in Figures 2c and 2f.

Notably, supershear ruptures in our model occur primarily via the direct transition mechanism, as shown in more detail in Figure 3. One exception occurs in a sequence with $a/b = 0.1$ and $L_{RA}/W = 0.1$ (Figure S6) in which a few early events transitioned to supershear ruptures at a higher S ratio as a result of sharp residual stress concentrations left by previous partial ruptures, as shown in Y. Liu and Lapusta (2008). However, this sequence eventually converges back to stable sub-Rayleigh ruptures after the effect of initial condition wanes. Figures 3a and 3b show the rupture speeds for both supershear and sub-Rayleigh events as a function of rupture propagation distance. For most supershear events, ruptures accelerate rapidly yet continuously to supershear speeds (direct transition), similar to those in C. Liu et al. (2014), without the mother-daughter crack transitional phase that defines the classic BA mechanism. An example of the direct supershear transition is demonstrated in Figures 3c and 3d, which clearly show the rupture accelerates to a supershear speed shortly after exiting the nucleation zone, without forming any daughter crack ahead of the primary rupture front. The very low S ratios (< 0.7, Figure 2f) for observed supershear events are consistent with the numerical study by C. Liu et al. (2014) who found direct supershear transition occurs at $S < 0.72$.

The evolution of rupture speed can be partially understood from recent theoretical developments. Using the numerically computed stress drops and fracture energies for a supershear event at $a/b = 0.1, L_{RA}/W = 0.4$ (black line in Figure 3a), we compute the predicted rupture speed (purple line) using theory developed by Kammer et al. (2018) and find it agrees qualitatively with the numerical results. Note that the applicability of that theory diminishes at propagation distances much larger than W (purple dashed line in Figure 3a), for which the finite fault width W limits the energy release rate (Weng & Ampuero, 2019, 2020). However, a formal equation of motion for a supershear rupture on elongated faults remains to be developed. We discuss the origin of the absence of mother-daughter crack mechanism in the next section.

Summary and Discussion

Our theoretical and simulation results show how frictional parameters and fault width W critically control the frequency of occurrence of supershear earthquakes throughout multiple earthquake cycles on a fault governed by rate-and-state friction. Particularly, a/b needs to be sufficiently low (< 0.4) and L_{RA}/W sufficiently high (0.2-1.2) for the fault to achieve a sufficiently high stress (low S ratio) to enable supershear transitions. Most supershear events are found to be induced by the direct transition mechanism (C. Liu et al., 2014; Kammer et al., 2018), which requires a very low S ratio (< 0.7). At large L_{RA}/W, the fault hosts weak partial ruptures and eventually transitions to aseismic slip.

The parameter range allowing supershear ruptures in our model is not common in laboratory frictional experiments. Although some experiments show negligible direct effect (very low a) during fast slip in mature mylonitic rock analogs (Takahashi et al., 2017), most others show that a and b are comparable in magnitude (Dieterich, 1978, 1979; Blanpied et al., 1998; Marone, 1998). Furthermore, the characteristic slip distance d_c is typically on the order of a few to tens of microns, which results in a nucleation size of a few meters (Dieterich, 1978; Blanpied et al., 1998), much smaller than the seismogenic width W ($\sim$10 km). Although seismologically inferred d_c values can be on the order of 0.1 m (e.g., Chen et al., 2021), this value is not representative of nucleation processes. The unusual friction properties required in our models may offer a clue on why supershear earthquakes are rare in nature. The key could be that frequent nucleation prevents sufficient stress accumulation during the inter-seismic period prior to a large earthquake, so that supershear transitions are difficult.

On the other hand, a few limitations of the current model, which we intentionally kept simple, may have restricted the permissible parameter range for supershear earthquakes. First of all, we neglected dynamic weakening at high slip rate, such as thermal pressurization (Viesca & Garagash, 2015) and shear heating (Rice, 2006), and assumed conventional rate-and-state friction for both nucleation and dynamic rupture. In theory, incorporating dynamic weakening in the form of strongly velocity-weakening friction (Text S4) should remove the restrictive effect of a/b on supershear transitions and can reduce the S ratio due to larger stress drop, but this remains to be studied in multi-cycle simulations.

In addition, we restricted our simulations to $L_{RA}/W > 0.1$ due to computational constraints. The first consequence of this assumption is that most of our simulations, excluding the partial ruptures cases at high L_{RA}/W, exhibit characteristic earthquake behavior (periodic whole-fault ruptures). However, when the nucleation length is further reduced ($L_{RA}/W \ll 0.1$) as required by laboratory data, partial ruptures with irregular recurrence emerge even on a simple fault with homogeneous frictional properties (Cattania, 2019). Chances are some earthquakes can jump from sub-Rayleigh to supershear rupture abruptly due to favorable residual stress concentration left by previous partial ruptures (Y. Liu & Lapusta, 2008), thus allowing supershear earthquakes at much higher S ratio. Similar scenarios could also happen due to other sources of heterogeneity, such as fault roughness, geometric complexities (bends, branches, and stepovers), and variable frictional properties. However, more frequent earthquake nucleation would also tend to keep the overall stress on the fault at a lower level. How the effects of frequent nucleation and stress heterogeneity play out in controlling the occurrence of supershear earthquakes deserves further work.

A large nucleation size also makes the classic mother-daughter crack transition more difficult. For a rupture to transition to a supershear speed through the mother-daughter crack mechanism, given an S ratio of 0.5, the supershear transition length L_{trans} must be larger than $\sim 20L_n$ in 2D and than $\sim 40L_n$ in an unbounded fault in 3D, according to Figure 5 in Dunham (2007). Dunham (2007) also found that a finite fault width W puts an upper bound on the supershear shear transition length $L_{trans} < 1.25$ W. For the mother-daughter crack supershear transition to be possible on a 3D bounded fault, W/L_n must be greater than ~ 32, which is outside the parameter range explored in our simulations. On the other hand, the direct supershear transition requires a dramatically shorter propagation distance $L_n/L \sim 0.3$ (see Figure 6 in C. Liu et al. (2014)) and thus it is the favored supershear transition mechanism observed in our simulations.

In summary, our current analysis, combining theory and simulations, marks an important first step to understand how the evolution of stress on long faults over multiple earthquake cycles affects their potential for hosting supershear earthquakes. Further work is warranted to extend the current analysis to more realistic friction laws including dynamic weakening, a more realistic nucleation size, inelastic off-fault behavior, and fault roughness and segmentation.

Acknowledgments

This work was funded by Université Côte d Azur through project PERFAULT-3D, supported by the French government through the UCAJEDI Investments in the Future project managed by the National Research Agency (ANR) with the reference number ANR-15-IDEX-01. Chao Liang is also supported by the Chinese government through the Fundamental Research Funds for the Central Universities disseminated by IDMR at Sichuan University. We thank Huihui Weng for inspiring discussions and suggestions. We also thank David Kammer for promptly providing the scripts for calculating the supershear rupture speeds on a 2D heterogeneous fault. Simulations were performed on the CEMEF cluster at Mines ParisTech.

Data Availability Statement

All data are generated by numerical simulations. The source code and input files associated with the simulation cases are contained in the Zenodo data repository (Liang et al., 2022). Our software uses PETSc (Balay et al., 2015) to solve large linear system in parallel, which is freely available at `https://petsc.org/release/`. The main version of the spectral element code SEM2DPACK (ref) is available at `https://github.com/jpampuero/sem2dpack`.

References

Abdelmeguid, M., Ma, X., & Elbanna, A. (2019). A novel hybrid finite element-spectral boundary integral scheme for modeling earthquake cycles: Application to rate and state faults with low-velocity zones. *Journal of Geophysical Research: Solid Earth*, *124*(12), 12854–12881. doi: 10.1029/2019JB018036

Andrews, D. (1976). Rupture velocity of plane strain shear cracks. *Journal of Geophysical Research*, *81*(32), 5679–5687. doi: 10.1029/JB081i032p05679

Balay, S., Abhyankar, S., Adams, M. F., Brown, J., Brune, P., Buschelman, K., ... Zhang, H. (2015). *PETSc users manual* (Tech. Rep. No. ANL-95/11 - Revision 3.6). Argonne National Laboratory. Retrieved from `http://www.mcs.anl.gov/petsc`

Bao, H., Ampuero, J.-P., Meng, L., Fielding, E. J., Liang, C., Milliner, C. W., ... Huang, H. (2019). Early and persistent supershear rupture of the 2018 magnitude 7.5 palu earthquake. *Nature Geoscience*, *12*(3), 200–205. doi: 10.1038/s41561-018-0297-z

Barbot, S. (2021). A spectral boundary-integral method for quasi-dynamic ruptures of multiple parallel faults. *Bulletin of the Seismological Society of America*, *111*(3), 1614–1630. doi: 10.1785/0120210004

Bizzarri, A., Dunham, E. M., & Spudich, P. (2010). Coherence of mach fronts during heterogeneous supershear earthquake rupture propagation: Simulations and comparison with observations. *Journal of Geophysical Research: Solid Earth*, *115*(B8). doi: 10.1029/2009JB006819

Blanpied, M., Marone, C., Lockner, D., Byerlee, J., & King, D. (1998). Quantitative measure of the variation in fault rheology due to fluid-rock interactions. *Journal of Geophysical Research: Solid Earth*, *103*(B5), 9691–9712. doi: 10.1029/98JB00162

Bouchon, M., & Vallée, M. (2003). Observation of long supershear rupture during the magnitude 8.1 kunlunshan earthquake. *Science*, *301*(5634), 824–826. doi: 10.1126/science.1086832

Bruhat, L., Fang, Z., & Dunham, E. M. (2016). Rupture complexity and the supershear transition on rough faults. *Journal of Geophysical Research: Solid Earth*, *121*(1), 210–224. doi: 10.1002/2015JB012512

Burridge, R. (1973). Admissible speeds for plane-strain self-similar shear cracks with friction but lacking cohesion. *Geophysical Journal International*, *35*(4), 439–455. doi: 10.1111/j.1365-246X.1973.tb00608.x

Cattania, C. (2019). Complex earthquake sequences on simple faults. *Geophysical Research Letters*, *46*(17-18), 10384–10393. doi: 10.1029/2019GL083628

Cattania, C., & Segall, P. (2019). Crack models of repeating earthquakes predict observed moment-recurrence scaling. *Journal of Geophysical Research: Solid Earth*, *124*(1), 476–503. doi: 10.1029/2018JB016056

Chen, X., Yang, H., & Jin, M. (2021). Inferring critical slip-weakening distance from near-fault accelerogram of the 2014 m w 6.2 ludian earthquake. *Seismological Society of America*, *92*(6), 3416–3427. doi: 10.1785/0220210089

Das, S. (2015). Supershear earthquake ruptures–theory, methods, laboratory experiments and fault superhighways: an update. In *Perspectives on european earthquake engineering and seismology* (pp. 1–20). Springer, Cham. doi: 10.1007/978-3-319-16964-4

Dieterich, J. H. (1978). Time-dependent friction and the mechanics of stick-slip. *Pure and Applied Geophysics*, *116*(4), 790–806. doi: 10.1007/BF00876539

Dieterich, J. H. (1979). Modeling of rock friction: 1. experimental results and constitutive equations. *Journal of Geophysical Research: Solid Earth*, *84*, 2161–2168. doi: 10.1029/JB084iB05p02161

Dunham, E. M. (2007). Conditions governing the occurrence of supershear ruptures under slip-weakening friction. *Journal of Geophysical Research: Solid Earth*, *112*(B7). doi: 10.1029/2006JB004717

Dunham, E. M., & Archuleta, R. J. (2004). Evidence for a supershear transient during the 2002 denali fault earthquake. *Bulletin of the Seismological Society of America*, *94*(6B), S256–S268. doi: 10.1785/0120040616

Dunham, E. M., Belanger, D., Cong, L., & Kozdon, J. E. (2011). Earthquake ruptures with strongly rate-weakening friction and off-fault plasticity, part 1: Planar faults. *Bulletin of the Seismological Society of America*, *101*(5), 2296–2307. doi: 10.1785/0120100075

Dunham, E. M., Favreau, P., & Carlson, J. (2003). A supershear transition mechanism for cracks. *Science*, *299*(5612), 1557–1559. doi: 10.1126/science.1080650

Ellsworth, W., Celebi, M., Evans, J., Jensen, E., Kayen, R., Metz, M., . . . Stephens, C. (2004). Near-field ground motion of the 2002 denali fault, alaska, earthquake recorded at pump station 10. *Earthquake spectra*, *20*(3), 597–615. doi: 10.1193/1.1778172

Erickson, B. A., Dunham, E. M., & Khosravifar, A. (2017). A finite difference method for off-fault plasticity throughout the earthquake cycle. *Journal of the Mechanics and Physics of Solids*, *109*, 50–77. doi: 10.1016/j.jmps.2017.08.002

Gabriel, A.-A., Ampuero, J.-P., Dalguer, L. A., & Mai, P. M. (2012). The transition of dynamic rupture styles in elastic media under velocity-weakening friction. *Journal of Geophysical Research: Solid Earth*, *117*(B09311). doi: 10.1029/2012JB009468

Hu, F., Oglesby, D. D., & Chen, X. (2019). The sustainability of free-surface-induced supershear rupture on strike-slip faults. *Geophysical Research Letters*, *46*(16), 9537–9543. doi: 10.1029/2019GL084318

Huang, Y., Ampuero, J.-P., & Helmberger, D. V. (2016). The potential for supershear earthquakes in damaged fault zones–theory and observations. *Earth and Planetary Science Letters*, *433*, 109–115. doi: 10.1016/j.epsl.2015.10.046

Kammer, D. S., Svetlizky, I., Cohen, G., & Fineberg, J. (2018). The equation of motion for supershear frictional rupture fronts. *Science Advances*, *4*(7), eaat5622. Retrieved from `https://www.science.org/doi/abs/10.1126/sciadv.aat5622` doi: 10.1126/sciadv.aat5622

Kaneko, Y., Ampuero, J.-P., & Lapusta, N. (2011). Spectral-element simulations of long-term fault slip: Effect of low-rigidity layers on earthquake-cycle dynamics. *Journal of Geophysical Research: Solid Earth*, *116*(B10313). doi: 10.1029/2011JB008395

Kaneko, Y., & Lapusta, N. (2010). Supershear transition due to a free surface in 3-d simulations of spontaneous dynamic rupture on vertical strike-slip faults. *Tectonophysics*, *493*(3-4), 272–284. doi: 10.1016/j.tecto.2010.06.015

Lapusta, N., & Liu, Y. (2009). Three-dimensional boundary integral modeling of spontaneous earthquake sequences and aseismic slip. *Journal of Geophysical Research: Solid Earth*, *114*(B9). doi: 10.1029/2008JB005934

Lehner, F. K., Li, V. C., & Rice, J. (1981). Stress diffusion along rupturing plate boundaries. *Journal of Geophysical Research: Solid Earth*, *86*(B7), 6155–6169. doi: 10.1029/JB086iB07p06155

Liang, C., Ampuero, J.-P., & Pino Munoz, D. (2022, January). *Dataset for*

"The paucity of supershear earthquakes on large faults governed by rate and state friction". Zenodo. Retrieved from https://doi.org/10.5281/zenodo.5832296 doi: 10.5281/zenodo.5832296

Liu, C., Bizzarri, A., & Das, S. (2014). Progression of spontaneous in-plane shear faults from sub-rayleigh to compressional wave rupture speeds. *Journal of Geophysical Research: Solid Earth*, *119*(11), 8331–8345. Retrieved from https://doi.org/10.1002/2014JB011187 doi: 10.1002/2014JB011187

Liu, D., Duan, B., & Luo, B. (2020). Eqsimu: a 3-d finite element dynamic earthquake simulator for multicycle dynamics of geometrically complex faults governed by rate-and state-dependent friction. *Geophysical Journal International*, *220*(1), 598–609. doi: 10.1093/gji/ggz475

Liu, Y., & Lapusta, N. (2008). Transition of mode ii cracks from sub-rayleigh to intersonic speeds in the presence of favorable heterogeneity. *Journal of the Mechanics and Physics of Solids*, *56*(1), 25–50. doi: 10.1016/j.jmps.2007.06.005

Liu, Y., & Rice, J. R. (2005). Aseismic slip transients emerge spontaneously in three-dimensional rate and state modeling of subduction earthquake sequences. *Journal of Geophysical Research: Solid Earth*, *110*(B8). doi: 10.1029/2004JB003424

Lu, X., Lapusta, N., & Rosakis, A. J. (2009). Analysis of supershear transition regimes in rupture experiments: the effect of nucleation conditions and friction parameters. *Geophysical Journal International*, *177*(2), 717–732. doi: 10.1111/j.1365-246X.2009.04091.x

Luo, Y., & Ampuero, J.-P. (2018). Stability of faults with heterogeneous friction properties and effective normal stress. *Tectonophysics*, *733*, 257–272. doi: 10.1016/j.tecto.2017.11.006

Marone, C. (1998). Laboratory-derived friction laws and their application to seismic faulting. *Annual Review of Earth and Planetary Sciences*, *26*(1), 643–696. doi: 10.1146/annurev.earth.26.1.643

Mello, M., Bhat, H., Rosakis, A., & Kanamori, H. (2014). Reproducing the supershear portion of the 2002 denali earthquake rupture in laboratory. *Earth and Planetary Science Letters*, *387*, 89–96. doi: 10.1016/j.epsl.2013.11.030

Meng, L., Zhang, A., & Yagi, Y. (2016). Improving back projection imaging with a novel physics-based aftershock calibration approach: A case study of the

2015 gorkha earthquake. *Geophysical Research Letters*, *43*(2), 628–636. doi: 10.1002/2015GL067034

Miyake, Y., & Noda, H. (2019). Fully dynamic earthquake sequence simulation of a fault in a viscoelastic medium using a spectral boundary integral equation method: does interseismic stress relaxation promote aseismic transients? *Earth, Planets and Space*, *71*(1), 1–12. doi: 10.1186/s40623-019-1113-8

Noda, H. (2021). Dynamic earthquake sequence simulation with a sbiem without periodic boundaries. *Earth, Planets and Space*, *73*(1), 1–10. doi: 10.1186/s40623-021-01465-6

Noda, H., & Lapusta, N. (2010). Three-dimensional earthquake sequence simulations with evolving temperature and pore pressure due to shear heating: Effect of heterogeneous hydraulic diffusivity. *Journal of Geophysical Research: Solid Earth*, *115*(B12). doi: 10.1029/2010JB007780

Noda, H., & Lapusta, N. (2013). Stable creeping fault segments can become destructive as a result of dynamic weakening. *Nature*, *493*(7433), 518–521. doi: 10.1038/nature11703

Ozawa, S., & Ando, R. (2021). Mainshock and aftershock sequence simulation in geometrically complex fault zones. *Journal of Geophysical Research: Solid Earth*, *126*(2), e2020JB020865. doi: 10.1029/2020JB020865

Rice, J. R. (2006). Heating and weakening of faults during earthquake slip. *Journal of Geophysical Research: Solid Earth*, *111*(B5). doi: 10.1029/2005JB004006

Richards-Dinger, K., & Dieterich, J. H. (2012). Rsqsim earthquake simulator. *Seismological Research Letters*, *83*(6), 983–990. doi: 10.1785/0220120105

Romanet, P., & Ozawa, S. (2021). Fully dynamic earthquake cycle simulations on a nonplanar fault using the spectral boundary integral element method (sbiem). *Bulletin of the Seismological Society of America*. doi: 10.1785/0120210178

Rosakis, A., Samudrala, O., & Coker, D. (1999). Cracks faster than the shear wave speed. *Science*, *284*(5418), 1337–1340.

Rubin, A. M. (2008). Episodic slow slip events and rate-and-state friction. *Journal of Geophysical Research: Solid Earth*, *113*(B11). doi: 10.1029/2008JB005642

Rubin, A. M., & Ampuero, J.-P. (2005). Earthquake nucleation on (aging) rate and state faults. *Journal of Geophysical Research: Solid Earth*, *110*(B11312). doi: 10.1029/2005JB003686

Ruina, A. (1983). Slip instability and state variable friction laws. *Journal of Geophysical Research: Solid Earth*, *88*(B12), 10359–10370. doi: 10.1029/JB088iB12p10359

Ryan, K. J., & Oglesby, D. D. (2014). Dynamically modeling fault step overs using various friction laws. *Journal of Geophysical Research: Solid Earth*, *119*(7), 5814–5829. doi: 10.1002/2014JB011151

Seki, J. (2017). *Development of Earthquake Cycle Simulation based on Spectral Element Method* (Unpublished master's thesis). Division of Earth and Planetary Sciences, Graduate School of Science, Kyoto University, Japan.

Takahashi, M., Van den Ende, M., Niemeijer, A., & Spiers, C. (2017). Shear localization in a mature mylonitic rock analog during fast slip. *Geochemistry, Geophysics, Geosystems*, *18*(2), 513–530. doi: 10.1002/2016GC006687

Templeton, E. L., & Rice, J. R. (2008). Off-fault plasticity and earthquake rupture dynamics: 1. dry materials or neglect of fluid pressure changes. *Journal of Geophysical Research: Solid Earth*, *113*(B9). doi: 10.1029/2007JB005529

Thakur, P., Huang, Y., & Kaneko, Y. (2020). Effects of low-velocity fault damage zones on long-term earthquake behaviors on mature strike-slip faults. *Journal of Geophysical Research: Solid Earth*, *125*(8), e2020JB019587. doi: 10.1029/2020JB019587

Vallée, M., & Dunham, E. M. (2012). Observation of far-field mach waves generated by the 2001 kokoxili supershear earthquake. *Geophysical Research Letters*, *39*(5). doi: 10.1029/2011GL050725

Viesca, R. C., & Garagash, D. I. (2015). Ubiquitous weakening of faults due to thermal pressurization. *Nature Geoscience*, *8*(11), 875–879. doi: 10.1038/ngeo2554

Vyas, J. C., Mai, P. M., Galis, M., Dunham, E. M., & Imperatori, W. (2018). Mach wave properties in the presence of source and medium heterogeneity. *Geophysical Journal International*, *214*(3), 2035–2052. doi: 10.1093/gji/ggy219

Weng, H., & Ampuero, J.-P. (2019). The dynamics of elongated earthquake ruptures. *Journal of Geophysical Research: Solid Earth*, *124*(8), 8584–8610. doi: 10.1029/2019JB017684

Weng, H., & Ampuero, J.-P. (2020). Continuum of earthquake rupture speeds enabled by oblique slip. *Nature Geoscience*, *13*(12), 817–821. doi: 10.1038/

s41561-020-00654-4

Weng, H., Huang, J., & Yang, H. (2015). Barrier-induced supershear ruptures on a slip-weakening fault. *Geophysical Research Letters*, *42*(12), 4824–4832. doi: 10.1002/2015GL064281

Wu, F. T., Thomson, K., & Kuenzler, H. (1972). Stick-slip propagation velocity and seismic source mechanism. *Bulletin of the Seismological Society of America*, *62*(6), 1621–1628. doi: 10.1785/BSSA0620061621

Xia, K., Rosakis, A., & Kanamori, H. (2005). Supershear and subrayleigh to supershear transition observed in laboratory earthquake experiments. *Experimental Techniques*, *29*(3), 63–66. doi: 10.1111/j.1747-1567.2005.tb00220.x

Xia, K., Rosakis, A. J., & Kanamori, H. (2004). Laboratory earthquakes: The subrayleigh-to-supershear rupture transition. *Science*, *303*(5665), 1859–1861. doi: 10.1126/science.1094022

Xu, J., Zhang, Z., & Chen, X. (2021). The effects of sediments on supershear rupture. *Tectonophysics*, *805*, 228777. doi: 10.1016/j.tecto.2021.228777

Xu, S., Ben-Zion, Y., & Ampuero, J.-P. (2012). Properties of inelastic yielding zones generated by in-plane dynamic ruptures—i. model description and basic results. *Geophysical Journal International*, *191*(3), 1325–1342. doi: 10.1111/j.1365-246X.2012.05679.x

Zeng, H., Wei, S., & Wu, W. (2020). Sources of uncertainties and artefacts in backprojection results. *Geophysical Journal International*, *220*(2), 876–891. doi: 10.1093/gji/ggz482

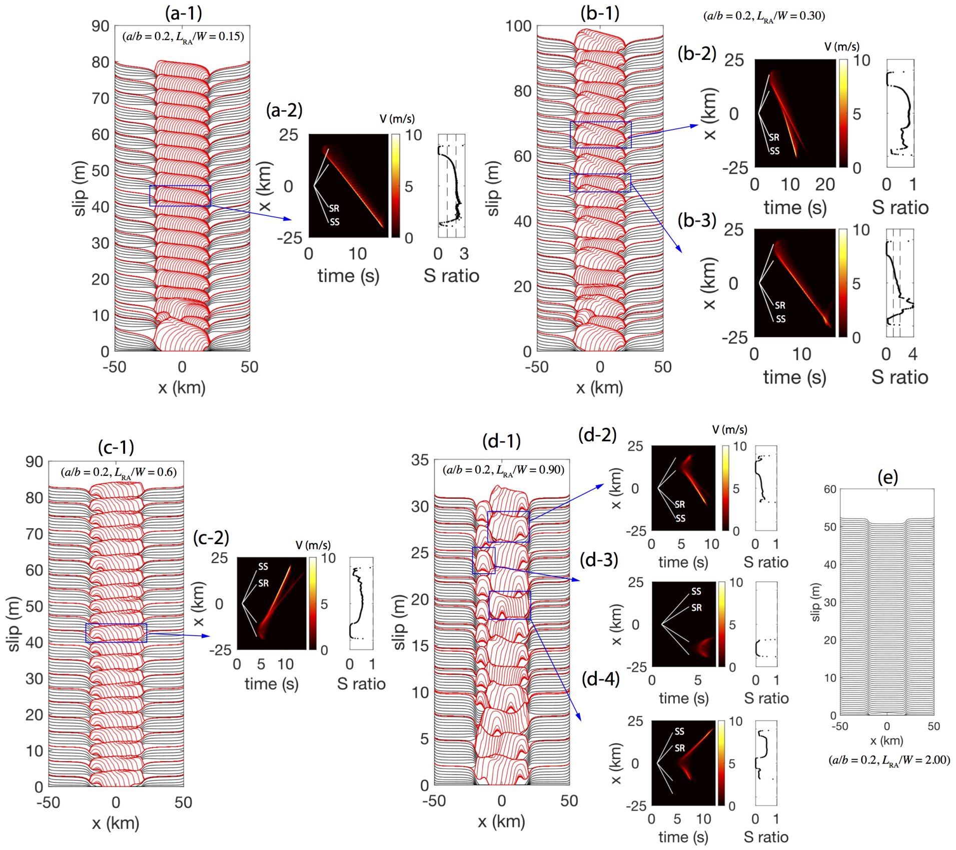

Figure 1. Rupture patterns in earthquake cycle simulations. Four cases are shown (a-d), with fixed $a/b = 0.2$ and varying L_{RA}/W as labeled. Each of the four panels shows: (left) cumulative slip, every ~0.3 s during coseismic phases (red) and every ~32 years during interseismic phases (black); (right) space-time distribution of slip rate V and S ratio of representative events. The slopes of the white lines in the space-time plots indicate speeds of super-shear (SS) and sub-Rayleigh (SR) rupture fronts. SS and SR events are also distinguishable by different spacing between the red curves in the cumulative slip plot. When increasing L_{RA}/W, the earthquake sequences experience a distinct transition in rupture style, from purely SR, to alternating SR and SS, to purely SS, to weak partial ruptures, and finally to aseismic slip.

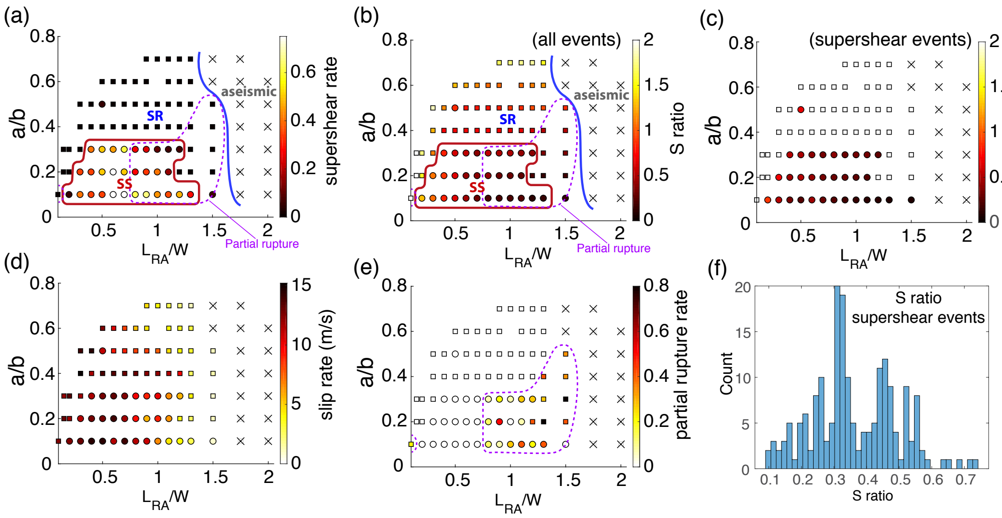

Figure 2. Rupture properties as a function of control parameters L_{RA}/W and a/b: (a) supershear occurrence rate, (b) median S ratio for all events, (c) median S ratio for supershear events, (d) peak slip rate, and (e) partial rupture rate. Each data point summarizes multiple earthquakes in a multi-cycle simulation. Circles indicate earthquake sequences with supershear (SS) ruptures, squares indicate pure sub-Rayleigh (SR) earthquake sequences, and crosses indicate aseismic sequences (peak slip rate < 0.01 m/s). The red and blue curves in (a) divide the parameter space into three "phases": SS, SR and aseismic. The purple dashed lines delineate the conditions for partial ruptures. (f) Histogram of the S ratio for supershear events. Most supershear events occur at $S < 0.7$.

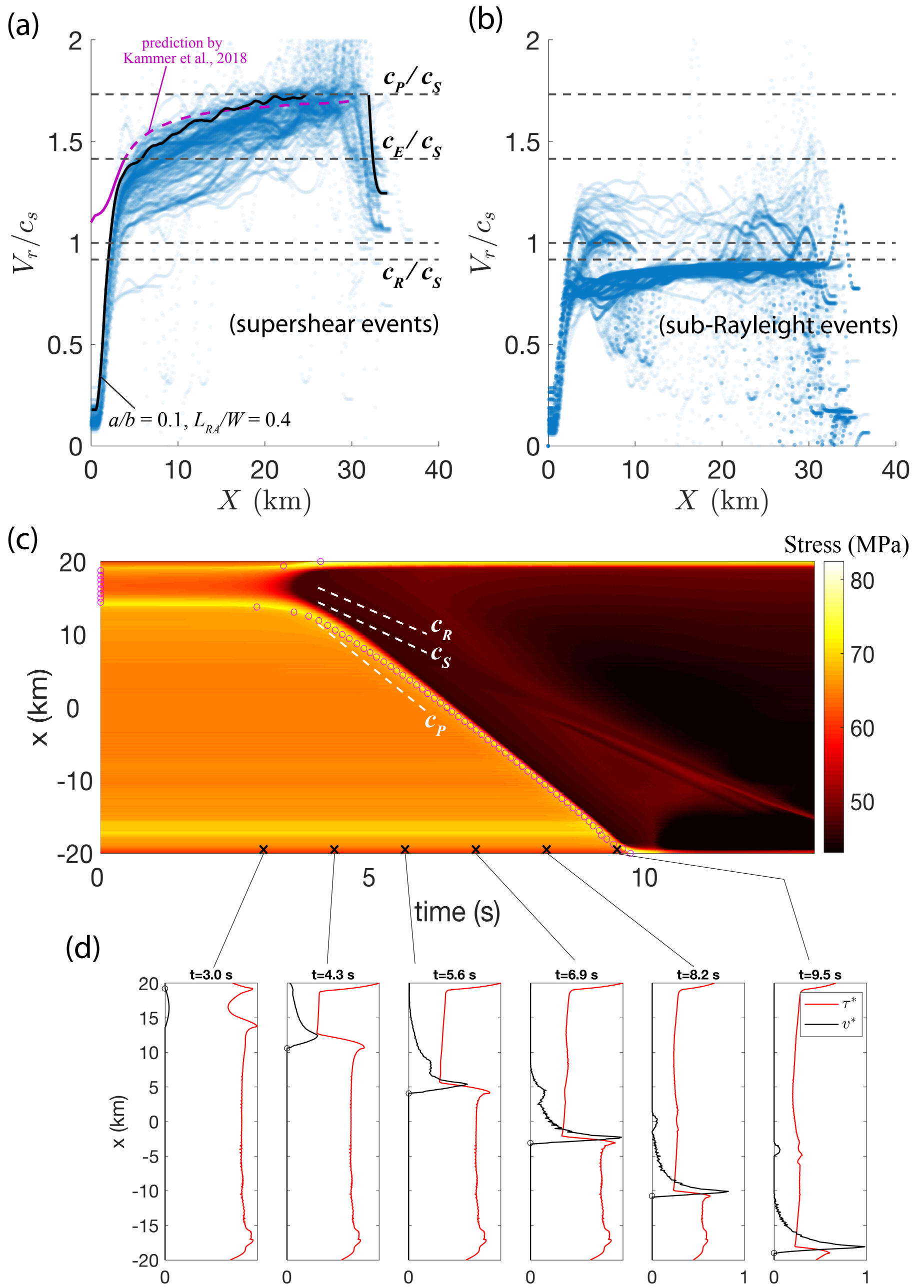

Figure 3. Normalized rupture speed V_r/c_s as a function of propagation distance outside of the nucleation zone for (a) supershear events and (b) sub-Rayleigh events. Most supershear ruptures occur via a direct supershear transition. The black solid line indicates the rupture speed of one supershear event with $a/b = 0.1, L_{RA}/W = 0.4$. The purple line indicates the predicted rupture speed of this event using the theory in Kammer et al. (2018). (c) Space-time distribution of fault shear stress τ of a supershear event indicated in (a), showing direct supershear transition. The purple circles mark the extracted rupture front. (d) Fault shear stress τ^* and slip rate v^* normalized by maximum values during the earthquake at different times. The black circle indicates the rupture front.

Supplementary material for “The paucity of supershear earthquakes on large faults governed by rate and state friction”

Chao Liang[1,2], Jean-Paul Ampuero[2], and Daniel Pino Muñoz[3]

[1]Institute for Disaster Management and Reconstruction (IDMR), Sichuan University, 610207, Chengdu, China

[2]Géoazur, Université Côte d’Azur (UCA), IRD, CNRS, Observatoire de la Côte d’Azur, 06560, Valbonne, France

[3]Centre de mise en forme des matériaux (CEMEF), Mines-ParisTech, PSL Research University, CNRS UMR 7635, 1 rue Claude Daunesse, 06904, Sophia Antipolis Cedex, France, France

Contents of this file

1. Text S1 to S4
2. Figures S1 to S5
3. Table S1

Introduction

In this supplementary file, we present the following:

- a description of the model
- a derivation of static stress intensity factors for 2.5D faults
- a derivation of S ratio on a rate and state fault

- a derivation of S ratio on a rate and state fault with strong velocity weakening

Text S1. Model description

We simulate earthquake cycles on a fault governed by rate-and-state friction, embedded in a homogeneous 2.5D plane strain elastic medium as shown in Figure S1. The fault is loaded by prescribing steady displacements on the remote boundaries and steady creep along the lateral extensions of the fault. This drives stable aseismic slip in the velocity strengthening (VS) region, which then loads the velocity weakening (VW) region where unstable ruptures occur. A 2.5D approximation is incorporated to account for a finite fault width W Weng and Ampuero (2019). We use the spectral element method (Kaneko et al., 2011) and a adaptive time stepper (Lapusta et al., 2000) to capture both the long-term quasi-static stress build up and short term dynamic rupture. However, different from Kaneko et al. (2011) who assumed an antiplane shear geometry, we consider two degree of freedoms per node to capture the in-plane shear. Seki (2017) first extended the algorithm in Kaneko et al. (2011) to 2D plane strain. However, his code is not parallelized, which limits its application for our study. We continued the development and parallelized the program using PETSc (Balay et al., 2015), which significantly accelerated the computation. Like Kaneko et al. (2011) and Seki (2017), we neglect inertia during interseismic periods, when the fault slip rate drops below a certain threshold ($\sim$0.01 m/s), and solve the full elastodynamics during coseismic periods. The readers are referred to Kaneko et al. (2011) and Seki (2017) for more details of the numerical algorithm. In this section, we briefly summarize the key governing equations in the model.

S1.1. Rate and state friction

We use laboratory-derived rate-and-state friction laws (Dieterich, 1978, 1979; Ruina, 1983) to describe the fault's resistance to sliding. These laws were developed from rock friction experiments at low slip rate. For a constant effective normal stress σ_n, the shear stress τ on the fault is related to slip rate V and a fault state variable θ by

$$\tau = \sigma_n \left[f_0 + a \ln\left(\frac{V}{V_0}\right) + b \ln\left(\frac{V_0 \theta}{d_c}\right) \right], \tag{S.1}$$

where a is a coefficient quantifying the direct effect of slip rate, b a coefficient quantifying the evolution effect of the state variable, f_0 is the reference frictional coefficient at steady state slip rate V_0, and d_c is the characteristic slip distance for state evolution. The state variable θ can be interpreted as an average age of asperities in contact on the sliding interface (Dieterich, 1978, 1979; Ruina, 1983). Two empirical state evolution laws are commonly used: aging law and slip law (Ruina, 1983). They exhibit the same asymptotic behavior in the vicinity of steady state but can differ considerably otherwise (Ampuero & Rubin, 2008). In this study, we work with the aging law

$$\frac{d\theta}{dt} = 1 - \frac{V\theta}{d_c}. \tag{S.2}$$

To remove the singularity of (S.1) at $V = 0$, we use the following regularized version (J. R. Rice & Ben-Zion, 1996; Lapusta et al., 2000)

$$\tau = a\sigma_n \ \mathrm{arcsinh}\left[\frac{V}{2V_0} \exp\left(\frac{f_0 + b\ln(V_0\theta/d_c)}{a} \right) \right], \tag{S.3}$$

which produces negligible change to equation (S.1) in the normal range of V and converges to $aV\sigma_n/2V_0$ when V is near zero. The frictional law is coupled to elasticity by enforcing that the fault shear stress should be equal to the shear strength predicted by rate and state friction. For this reason, we use shear "stress" and "strength" interchangeably.

For the numerical model to be sufficiently accurate, both the process zone and the nucleation size need to be resolved (Lapusta et al., 2000). For 2D plane strain geometry, the static process zone size R_0 (Lapusta et al., 2000) is

$$R_0 = \frac{9\pi}{32}\frac{G^* d_c}{b\sigma_n} \tag{S.4}$$

where $G^* = G/(1-\nu)$, G is shear modulus, ν is Poisson's ratio. Two theoretical estimates of nucleation length exist for 2D plane strain geometry (J. R. Rice & Ruina, 1983; Rubin & Ampuero, 2005)

$$L_{RR} = \frac{\pi}{4}\frac{G^* d_c}{\sigma_n(b-a)}, \tag{S.5}$$

$$L_{RA} = \frac{\pi}{2}\frac{G^* d_c b}{\sigma_n(b-a)^2}. \tag{S.6}$$

The former estimate L_{RR} is derived from linear stability analysis of perturbations to steady sliding (J. R. Rice & Ruina, 1983) and L_{RA} is derived from a fracture mechanics energy balance (Rubin & Ampuero, 2005). When $a/b > 0.5$, L_{RA} is more appropriate.

S1.2. 2.5D approximation

We use the 2.5D approximation formalised by Lehner, Li, and Rice (1981) to capture the lithosphere/asthenosphere coupling due to slip on a fault with a finite width W. The full formulation in Lehner et al. (1981) treats the asthenosphere as a Maxwell viscoelastic material. In our work, we only keep the elastic part and assume a homogeneous elastic modulus. Considering a finite fault width W, the thickness-averaged equation of momentum balance in the seismogenic layer is

$$\rho\ddot{u}_i = \sigma_{ij,j} - r_i, \tag{S.7}$$

where ρ is density, u_i is the thickness-averaged displacement in two horizontal directions x ($i = 1$) and y ($i = 2$), σ_{ij} is the depth-averaged Cauchy stress tensor, and r_i is the additional resistance added by the finite fault width W

$$r_i = G \frac{u_i}{(\gamma W)^2}. \tag{S.8}$$

The constant γ takes different values for different geometries: $1/\pi$ for a fault embedded in unbounded space and $2/\pi$ for a shallow fault in elastic halfspace (Weng & Ampuero, 2019). As shown in Weng and Ampuero (2019), this 2.5D approximation is a very good representation of the 3D problem in terms of energy release rate given the fault length L is sufficiently greater than W.

Note that u_i needs to be understood as the relative displacement between the upper lithosphere which the fault cuts through, and the lower asthenosphere. During interseisic periods, when the non-creeping section of the fault is locked, stress can build up in the middle of the locked region due to the loading from the bottom which creeps at the long term plate rate V_{pl}. For elongated faults, the fault stressing rate in mode II is

$$\dot{\tau} = C_s G V_{pl}/W, \tag{S.9}$$

where V_{pl} is plate rate and the constant C_s is $4/\pi$ for buried faults and $2/\pi$ for shallow surface faults. In our study, we assume a shallow surface fault, namely, $\gamma = 2/\pi$ and $C_s = 2/\pi$.

Text S2. Static stress intensity factors (SIF)

In this section, we give heuristic expressions of static SIFs in 2.5D which will be used to derive the inter-event slip δ_n or time t_n in the next section. By "heuristic", we mean these formula are not derived analytically from first principles but are shown to converge to solutions of 2D plane strain and 2.5D long faults as we take the two limits $W \to \infty$ and $W \to 0$, respectively. This approach is acceptable because our primary goal here is not to derive an exact formula, but to obtain expressions useful for identifying key dimensionless parameters and guiding the design and analysis of our numerical simulations.

Consider a crack at $x \in (0, l)$ with the crack tip at $x = l$ and connected to a semi-infinite dislocation at $x \in (-\infty, 0)$. The loading on the crack is a constant slip δ in $x \in (-\infty, 0)$ and a constant stress change $\Delta\tau$ in $x \in (0, l)$. This is the approximate loading condition for a slowly propagating crack in the velocity weakening region driven by steady creep in the velocity strengthening region (Cattania, 2019; Cattania & Segall, 2019). The SIF K at the crack tip can be written as the sum of two SIFs

$$K(l) = K_\delta(l) - K_{\Delta\tau}(l), \tag{S.10}$$

where K_δ is the SIF from a constant slip δ in $x \in (-\infty, 0)$ and a zero stress change in $x \in (0, l)$, and $K_{\Delta\tau}$ is the SIF from zero slip in $x \in (-\infty, 0)$ and a stress change $\Delta\tau$ in $x \in (0, l)$. The negative sign comes from the fact that a positive stress change $\Delta\tau$ drives the crack tip to deform in the opposite sense to that from a positive slip.

S2.1 Solution for $K_{\Delta\tau}$

We first seek a solution for $K_{\Delta\tau}$. The known solution in 2D plane strain (Tada et al., 2000; Cattania, 2019) is

$$K^{2D}_{\Delta\tau}(l) = \Delta\tau\sqrt{\pi l/2}. \tag{S.11}$$

Unfortunately, the analytical solution for 2.5 D in such a loading condition does not exist. However, from Weng and Ampuero (2019), we can obtain the static SIF for a uniform stress change inside the crack and zero stress change in the semi-infinite tail by setting the rupture speed to zero:

$$K_{\Delta\tau}^{25D,*}(l) = \Delta\tau\sqrt{2\gamma W}\text{erf}\left\{\sqrt{l/(\gamma W)}\right\}, \tag{S.12}$$

where erf(x) is the error function. In the limit $l \gg W$, the importance of detailed loading in the semi-infinite tail diminishes and we must have $K_{\Delta\tau} \to K_{\Delta\tau}^{25D,*}$. In light of this solution, we assume the expression of $K_{\Delta\tau}$ is in a similar form:

$$K_{\Delta\tau}(l) = A_1\Delta\tau\sqrt{2\gamma W}\text{erf}\left\{A_2\sqrt{l/(\gamma W)}\right\}, \tag{S.13}$$

In the limit $l \gg W$, we require $K_{\Delta\tau} \to K_{\Delta\tau}^{25D,*}$, thus $A_1 = 1$. In the limit $l \ll W$, we require $K_{\Delta\tau} \to K_{\Delta\tau}^{2D}$, which gives $A_2 = \pi/4$. Therefore, we obtain

$$K_{\Delta\tau}(l) = \Delta\tau\sqrt{2\gamma W}\text{erf}\left\{\frac{\pi}{4}\sqrt{l/(\gamma W)}\right\}. \tag{S.14}$$

This expression provides a smooth interpolation between $K_{\Delta\tau}^{25D,*}$ and $K_{\Delta\tau}^{2D}$.

S2.2 Solution for K_δ

Next, we seek a solution for K_δ. The known 2D plane strain solution is (Tada et al., 2000; Cattania, 2019)

$$K_\delta^{2D}(l) = \frac{1}{\sqrt{2\pi}}\frac{G^*\delta}{\sqrt{l}}, \tag{S.15}$$

where $G^* = G/(1-\nu)$ and ν is the Poisson's ratio. From equation (55) in Weng and Ampuero (2019) we obtain the SIF for a zero stress in the the crack $x \in (0, l)$ and constant stress change $\Delta\tau$ in the semi-infinite tail $x \in (-\infty, 0)$ as

$$K_\delta^{25D,*}(l) = \Delta\tau\sqrt{2\gamma W}\text{erfc}\left\{\sqrt{l/(\gamma W)}\right\}, \tag{S.16}$$

where $\text{erfc}(x) = 1 - \text{erf}(x)$ is the complementary error function and $\Delta\tau$ is linked to slip δ in the semi-infinite tail by

$$\Delta\tau(l) = C_s G\delta/W \tag{S.17}$$

for a long crack. It is clear that in the long fault limit, $l \gg W$, we have $K_\delta^{25D,*} \propto G\delta/\sqrt{W}$ and quickly decays as l/W increases. Using a similar the strategy as that in obtaining $K_{\Delta\tau}$, we assume K_δ to have the following form:

$$K_\delta(l) = C_1 \frac{G^*\delta}{\sqrt{\gamma W}\text{erf}\left\{C_2\sqrt{l/(\gamma W)}\right\}}\text{erfc}\left\{\sqrt{l/(\gamma W)}\right\}. \tag{S.18}$$

Now, requiring $K_\delta \to K_\delta^{25D,*}$ in the limit $l/W \gg 1$ and $K_\delta \to K_\delta^{2D}$ in the limit $l/W \ll 1$, we obtain the two constants

$$C_1 = \sqrt{2}C_s\gamma(1-\nu) \tag{S.19}$$

$$C_2 = \pi C_s\gamma(1-\nu). \tag{S.20}$$

Recall that C_s and γ are $4/\pi$ and $1/\pi$ for buried faults, and $2/\pi$ and $2/\pi$ for shallow surface faults. We have $C_s\gamma = 4/\pi^2$. For Poisson solid $\nu = 0.25$, we have $C_1 \approx 0.429$ and $C_2 \approx 0.955$.

Text S3. *S* ratio on a rate and state fault

With the results from the previous section, we are now ready to derive the S ratio for a characteristic earthquake event on a rate and state fault, which is the most important parameter that controls the occurrence rate of supershear earthquakes in our model. We consider a velocity weakening (VW) patch surrounded by velocity strengthening (VS) region, similar as Cattania (2019) but on an elongated fault.

The S ratio is defined as

$$S = \frac{\tau_p - \tau_0}{\tau_0 - \tau_r} = \frac{\tau_p - \tau_r}{\tau_0 - \tau_r} - 1, \tag{S.21}$$

where τ_p, τ_r, and τ_0 are the peak, residual and initial shear stress on the fault for a characteristic earthquake, which we shall estimate in the following subsections.

S3.1. stresses

Using the rate and state friction law, equation (S.1), we can write

$$\tau_p = \sigma_n \left[f_0 + a \ln\left(\frac{V_{co}}{V_0}\right) + b \ln\left(\frac{V_0 \theta_i}{d_c}\right) \right], \tag{S.22}$$

$$\tau_r = \sigma_n \left[f_0 + (a-b) \ln\left(\frac{V_{co}}{V_0}\right) \right], \tag{S.23}$$

where V_{co} is the peak slip rate during the earthquake and θ_i is the state variable just prior to the earthquake. V_{co} is typically on the order of 1-10 m/s. An adequate order of magnitude estimate is given by $V_{dyn} = 2C_s a\sigma_n/G$ (Rubin & Ampuero, 2005). During coseismic slip, the state variable θ rapidly drops to a value comparable to $d_c/V_{co} \ll 1$ s. Over the inter-seismic period, the VW part of the fault slides at an extremely low slip rate, effectively locked, and the state variable increases linearly with time. Therefore, $\theta_i = T_n$, the inter-event loading time during which aseismic creep slowly propagates into the VW patch from the VS region. We re-write τ_p as

$$\tau_p = \sigma_n \left[f_0 + a \ln\left(\frac{V_{co}}{V_0}\right) + b \ln\left(\frac{V_0 T_n}{d_c}\right) \right]. \tag{S.24}$$

The initial stress prior to an earthquake is

$$\tau_0 = \tau_r + \dot{\tau} T_n, \tag{S.25}$$

where $\dot{\tau}$ is the stressing rate expressed in equation (S.9). Using equations (S.9), (S.24), (S.23) and (S.25), we get

$$S = \frac{\sigma_n W b \ln\left(V_{co} T_n / d_c\right)}{C_s G V_{pl} T_n} - 1. \tag{S.26}$$

The final task is to estimate the inter-event time T_n.

S3.2. Inter-event time T_n

We follow the method in Cattania (2019) to estimate T_n. At the propagating crack tip, the total SIF must balance the fracture toughness K_c. Using equation S.10, we have

$$K_\delta(l) - K_{\Delta\tau} = K_c. \tag{S.27}$$

During interseismic periods, the slip rate behind the slowly propagating crack tip is small, implying K_c is negligible, and we have

$$K_\delta(l) = K_{\Delta\tau}. \tag{S.28}$$

Substituting equations (S.18) and (S.18) into (S.28), we have

$$\delta = \eta\left(\frac{l}{\gamma W}\right)\delta_{2D}, \tag{S.29}$$

where

$$\delta_{2D} = \frac{\pi \Delta\tau l}{G^*} \tag{S.30}$$

and

$$\eta(\xi) = \frac{\sqrt{2}}{C_1 \pi}\frac{1}{\xi}\frac{\mathrm{erf}(\pi\sqrt{\xi}/4)\mathrm{erf}(C_2\sqrt{\xi})}{\mathrm{erfc}(\sqrt{\xi})}. \tag{S.31}$$

The coefficients C_1 and C_2 are given in equations (S.19) and (S.20), respectively. δ is the amount of slip in the semi-infinite tail needed for a crack to advance by l with constant stress change of $\Delta\tau$ within the crack $x \in (0, l)$. η denotes the difference between the 2.5D and 2D results, which converges to 1 as $\xi \to +0$ and diverges at large ξ. The shape of $\eta(\xi)$ is plotted in Figure S2.

Since the semi-infinite tail is steadily creeping at plate rate V_{pl}, the inter-event time T_n is the time needed for the semi-infinite tail to accumulate sufficient slip so that the crack length in the VW region reaches a critical nucleation length L_n for instability. Thus,

$$T_n = \eta(L_n/\gamma W)\frac{\pi \Delta\tau L_n}{G^* V_{pl}}. \tag{S.32}$$

The stress change in the propagating creeping patch in the VW region can be estimated as

$$\Delta\tau = \tau_c - \tau_r^n = \sigma_n(b-a)\ln\left(\frac{V_{co}^n}{V_{pl}}\right), \tag{S.33}$$

where the τ_c is the steady state stress when the VW patch is creeping at plate rate V_{pl}, τ_r^n and V_{co}^n are the residual stress and peak slip rate during the previous earthquake inside the nucleation patch. We make a distinction between τ_r^n, V_{co}^n and τ_r,V_{co} because the residual stress and peak slip rate along a finite fault is generally non-uniform. V_{co} and τ_r should be understood as representative values for the entire dynamic rupture of the previous earthquake, where the nucleation phase is only a small portion. On the other hand, peak slip rate is lower inside the nucleation patch than outside it, $V_{co}^n < V_{co}$, and also not sensitive to the maximum rupture speed, as shown in Figure S4.

Substituting (S.33) into (S.32), we obtain

$$T_n = \eta\pi\frac{\sigma_n}{G^*}\frac{L_n}{V_{pl}}(b-a)\ln\left(\frac{V_{co}^n}{V_{pl}}\right) \tag{S.34}$$

Finally, substituting (S.34) into (S.26), we have

$$S = \alpha\frac{1}{C_s(1-\nu)\pi}\frac{1}{\eta}\frac{1}{1-a/b}\frac{W}{L_n} - 1, \tag{S.35}$$

where

$$\alpha = \frac{\ln\left(V_{co}T_n/d_c\right)}{\ln\left(\frac{V_{co}^n}{V_{pl}}\right)}. \tag{S.36}$$

From (S.35), it is clear that S is dominantly controlled by two dimensionless parameters: a/b and W/L_n. Since η is a monotonically increasing function of L_n/W, either decreasing a/b or W/L_n leads to a lower S ratio, which favors supershear transition.

The parameter α depends also on a/b and L_n through T_n but the dependency is weak due to the presence of logarithms. Within one seismic sequence, a supershear event has a higher coseismic slip rate V_{co} but similar V_{co}^n compared to a sub-Rayleigh event. This leads to an oscillation of α and S ratio, which under certain conditions leads to the alternation of supershear and sub-Rayleigh events as shown in Figure 1 in the main text and Figure S4.

Due to the deviation from 2D plane strain and from the small process zone assumption, L_n is generally unknown before numerical simulation but is proportional to 2D nucleation lengths. However, as shown in Figure S3, L_{RR} or L_{RA} are only close to L_n when $L_n \ll W$ and $R_0 \ll W$. Otherwise, L_n is generally larger than L_{RR} or L_{RA}. With the parameter values explored in our study, the maximum L_n/L_{RA} is less than 7 (see Figure S3). Nonetheless, L_{RR} or L_{RA} are still good scales for L_n. In our simulations, we scan the parametric space by varying L_{RA}/W and keeping R_0 fixed.

Now, we can write equation (S.34) using L_{RA} as

$$T_n = \eta\frac{\pi^2}{2}\frac{1}{1-a/b}\frac{d_c}{V_{pl}}\frac{L_n}{L_{RA}}\ln\left(\frac{V_{co}}{V_{pl}}\right) \tag{S.37}$$

Using (S.37), we have

$$\ln\left(V_{co}T_n/d_c\right) = \ln\left(\eta\frac{\pi^2}{2}\frac{1}{1-a/b}\right) + \ln\left(\frac{V_{co}}{V_{pl}}\right) + \ln\left(\frac{L_n}{L_{RA}}\right) + \ln\left[\ln\left(\frac{V_{co}}{V_{pl}}\right)\right]. \tag{S.38}$$

It is informative to plug in some typical values. Let us assume $V_{co} \sim 10$ m/s, $V_{co}^n \sim 2$ m/s, $V_{pl} \sim 10^{-10}$ m/s (3 mm/year), $L_n/L_{RA} \sim [1,7]$, $\eta\frac{\pi^2}{2}\frac{1}{1-a/b} \sim [1,10000]$. We have $\ln(V_{co}/V_{pl}) \sim 25.3$, $\ln(V_{co}^n/V_{pl}) \sim 23.7$, $\ln[\ln(V_{co}/V_{pl})] \sim 3.2$, $\ln(L_n/L_{RA}) \sim [0,1.9]$, $\ln\left(\eta\frac{\pi^2}{2}\frac{1}{1-a/b}\right) \sim [0,9.2]$. The value of α is

$$\alpha = \frac{\ln(V_{co}T_n/d_c)}{\ln(V_{co}^n/V_{pl})} = \frac{25.3 + 3.2 + [0,1.9] + [0,9.2]}{23.7} = [1.13, 1.56]. \tag{S.39}$$

Text S4. *S* ratio on rate and state fault with strongly velocity weakening

Although we do not consider dynamic weakening in our numerical simulation, we derive an expression for the S ratio for a rate and state friction law with strong velocity-weakening without thermal pressurization. At low slip rate, we assume nucleation is well captured by the conventional rate and state friction with the aging law. The strongly velocity weakening model is motivated by flash heating at high slip rate, for which various formulations exist (J. Rice, 1999; Beeler et al., 2008; Ampuero & Ben-Zion, 2008; Gabriel et al., 2012; Dunham et al., 2011). Regardless of different formulations, the common feature is that the friction coefficient reduces to a drastically weakened value f_w at slip rates higher than a weakening slip rate V_w.

During the earthquake, the shear stress is assumed to increase from the initial stress τ_0 to peak stress τ_p with negligible state evolution. At this stage, strongly velocity weakening has not yet taken effect and τ_p has the same expression as in (S.24).

Due to the high slip rate $V_{co} \gg V_w$, shear stress on the fault rapidly drops and evolves towards the fully weakened value

$$\tau_r = \sigma_n f_w. \tag{S.40}$$

During the inter-seismic period, stress is accumulated again and

$$\tau_0 - \tau_r = \dot{\tau} T_n = C_s G V_{pl} T_n / W \tag{S.41}$$

Therefore, we can write S as

$$S = \frac{\sigma_n \left[f_0 - f_w + a \ln\left(\frac{V_{co}}{V_0}\right) + b \ln\left(\frac{V_0 T_n}{d_c}\right)\right]}{C_s G V_{pl} T_n / W} - 1. \tag{S.42}$$

The final task is to estimate T_n. For simplicity, we assume the same coseismic slip rate in the nucleation patch. According to equation (S.32), the question boils down to estimating the stress change $\Delta\tau$ in the creeping patch in the velocity weakening region. Inside this creeping patch, the fault slides steadily at V_{pl} and the shear stress is

$$\tau_c = \sigma_n [f_0 + (b-a) \ln(V_0/V_{pl})]. \tag{S.43}$$

Therefore, we have

$$\Delta\tau = \tau_c - \tau_r = \sigma_n \left[f_0 - f_w + (b-a) \ln(V_0/V_{pl}) \right]. \tag{S.44}$$

Using equation (S.32), we have

$$T_n = \eta \frac{\pi L_n \sigma_n}{G^* V_{pl}} \left[f_0 - f_w + (b-a) \ln(V_0/V_{pl}) \right]. \tag{S.45}$$

Substituting (S.45) into (S.42), we obtain

$$S = \frac{1}{\eta} \frac{\beta}{C_s (1-\nu) \pi} \frac{W}{L_n} - 1, \tag{S.46}$$

where

$$\beta = 1 + \frac{a \ln\left(\frac{V_{co}}{V_{pl}}\right) + b \ln\left(\frac{V_{pl} T_n}{d_c}\right)}{f_0 - f_w + (b-a) \ln(V_0/V_{pl})}. \tag{S.47}$$

On one hand, W/L_n is still an important dimensionless parameter that controls S, similar to the case of conventional rate and state friction (S.35). This is due to the direct influence of the nucleation length L_n on the inter-event time T_n, which then controls $\tau_0 - \tau_r$. On the other hand, the dependence of other frictional parameters, such as $f_0 - f_w$, a, b, are encapsulated in the parameter β. Taking reasonable values for $V_0 \sim 10^{-6}$ m/s, $V_{pl} \sim 10^{-10}$ m/s, $V_{co} \sim 10$ m/s, $b \sim$0.01, $a \sim 0.1 - 0.9\ b$, $f_0 \sim 0.6$, $f_w \sim 0.15$, $T_n \sim 1 - 1000$ years, $d_c \sim 10^{-6} - 10^{-3}$ m, β varies between 1.1 to 1.8. Due to the dominance of $f_0 - f_w$ over other terms, β is not very sensitive to the values of a or b. As a result, the S ratio in equation (S.46) is also less sensitive to a compared to the conventional rate and state friction (equation S.35). In particular, the scaling parameter related to a for conventional rate and state friction is $\frac{1}{1-a/b}$, which significantly amplifies the S ratio at high a/b and makes supershear transition difficult. However, this effect no longer exists after incorporating strongly velocity weakening, which helps to reduce the S ratio, especially at high a/b, and therefore favors supershear transition.

References

Ampuero, J.-P., & Ben-Zion, Y. (2008). Cracks, pulses and macroscopic asymmetry of dynamic rupture on a bimaterial interface with velocity-weakening friction. *Geophysical Journal International*, *173*(2), 674–692. doi: 10.1111/j.1365-246X.2008.03736.x

Ampuero, J.-P., & Rubin, A. M. (2008). Earthquake nucleation on rate and state faults–aging and slip laws. *Journal of Geophysical Research: Solid Earth*, *113*(B1). doi: 10.1029/2007JB005082

Balay, S., Abhyankar, S., Adams, M. F., Brown, J., Brune, P., Buschelman, K., … Zhang, H. (2015). *PETSc users manual* (Tech. Rep. No. ANL-95/11 - Revision 3.6). Argonne National Laboratory. Retrieved from `http://www.mcs.anl.gov/petsc`

Beeler, N., Tullis, T., & Goldsby, D. (2008). Constitutive relationships and physical basis of fault strength due to flash heating. *Journal of Geophysical Research: Solid Earth*, *113*(B1). doi: 10.1029/2007JB004988

Cattania, C. (2019). Complex earthquake sequences on simple faults. *Geophysical Research Letters*, *46*(17-18), 10384–10393. doi: 10.1029/2019GL083628

Cattania, C., & Segall, P. (2019). Crack models of repeating earthquakes predict observed moment-recurrence scaling. *Journal of Geophysical Research: Solid Earth*, *124*(1), 476–503. doi: 10.1029/2018JB016056

Dieterich, J. H. (1978). Time-dependent friction and the mechanics of stick-slip. *Pure and Applied Geophysics*, *116*(4), 790–806. doi: 10.1007/BF00876539

Dieterich, J. H. (1979). Modeling of rock friction: 1. experimental results and constitutive equations. *Journal of Geophysical Research: Solid Earth*, *84*, 2161–2168. doi: 10.1029/JB084iB05p02161

Dunham, E. M., Belanger, D., Cong, L., & Kozdon, J. E. (2011). Earthquake ruptures with strongly rate-weakening friction and off-fault plasticity, part 1: Planar faults. *Bulletin of the Seismological Society of America*, *101*(5), 2296–2307. doi: 10.1785/0120100075

Gabriel, A.-A., Ampuero, J.-P., Dalguer, L. A., & Mai, P. M. (2012). The transition of dynamic rupture styles in elastic media under velocity-weakening friction. *Journal of Geophysical Research: Solid Earth*, *117*(B09311). doi: 10.1029/2012JB009468

Kaneko, Y., Ampuero, J.-P., & Lapusta, N. (2011). Spectral-element simulations of long-term fault slip: Effect of low-rigidity layers on earthquake-cycle dynamics. *Journal* *of Geophysical Research: Solid Earth*, *116*(B10313). doi: 10.1029/2011JB008395

Lapusta, N., Rice, J. R., Ben-Zion, Y., & Zheng, G. (2000). Elastodynamic analysis for slow tectonic loading with spontaneous rupture episodes on faults with rate-and state-dependent friction. *Journal of Geophysical Research: Solid Earth*, *105*(B10), 23765–23789. doi: 10.1029/2000JB900250

Lehner, F. K., Li, V. C., & Rice, J. (1981). Stress diffusion along rupturing plate boundaries. *Journal of Geophysical Research: Solid Earth*, *86*(B7), 6155–6169. doi: 10.1029/JB086iB07p06155

Rice, J. (1999). Flash heating at asperity contacts and rate-dependent friction. *Eos Trans. AGU*, *80*(46), F471.

Rice, J. R., & Ben-Zion, Y. (1996). Slip complexity in earthquake fault models. *Proceedings of the National Academy of Sciences*, *93*(9), 3811–3818. doi: 10.1073/pnas.93.9.3811

Rice, J. R., & Ruina, A. L. (1983, 06). Stability of Steady Frictional Slipping. *Journal of Applied Mechanics*, *50*(2), 343-349. doi: 10.1115/1.3167042

Rubin, A. M., & Ampuero, J.-P. (2005). Earthquake nucleation on (aging) rate and state faults. *Journal of Geophysical Research: Solid Earth*, *110*(B11312). doi: 10.1029/2005JB003686

Ruina, A. (1983). Slip instability and state variable friction laws. *Journal of Geophysical Research: Solid Earth*, *88*(B12), 10359–10370. doi: 10.1029/JB088iB12p10359

Seki, J. (2017). *Development of Earthquake Cycle Simulation based on Spectral Element Method* (Unpublished master's thesis). Division of Earth and Planetary Sciences, Graduate School of Science, Kyoto University, Japan.

Tada, H., Paris, P. C., & Irwin, G. R. (2000). *The stress analysis of cracks handbook.* New York: ASME Press.

Weng, H., & Ampuero, J.-P. (2019). The dynamics of elongated earthquake ruptures. *Journal of Geophysical Research: Solid Earth*, *124*(8), 8584–8610. doi: 10.1029/2019JB017684

Table S1. Material parameters

Parameter	Symbol	Value
Fixed parameters		
Total domain width	H	40 km
Total domain length	LF	120 km
Length of VW segment	L	40 km
Length of each (of two) VS segment	L_{VS}	30 km
2.5D shape constant	γ	$2/\pi$
2.5D loading constant	C_s	$2/\pi$
Plate rate	V_{pl}	10^{-9} m/s
S wave speed	c_s	3464 m/s
P wave speed	c_p	6400 m/s
Density	ρ	2670 m/s
Effective normal stress	σ_n	100 MPa
Initial shear stress	τ_0	50 MPa
Rate and state parameter b	b	0.01
Characteristic slip distance	d_c	0.053 m[a]
Static process zone size	R_0	2 km
Reference friction coefficient	f_0	0.6
Reference slip rate	V_0	10^{-6} m/s
Initial slip rate	V_{ini}	10^{-9} m/s
Spectral element size	h	500 m
Gauss-Lobatto-Legendre nodes per element	$ngll$	5
slip rate threshold (switch static to dynamic)	V_{S2D}	0.05 m/s
slip rate threshold (switch dynamic to static)	V_{D2S}	0.02 m/s
Varied parameters		
Fault width	W	2 to 10 km[b]
Rate and state parameter a	a	0.001 to 0.007

[a]This value is used in the VW region such that $R_0 = 2$ km given other parameters. d_c in the VS region is assumed to be 0.53 m.
[b]W is varied such that L_{RA}/W takes the desired values from 0.1 to 2.0. Cases are rejected if W falls out of 2-10 km.

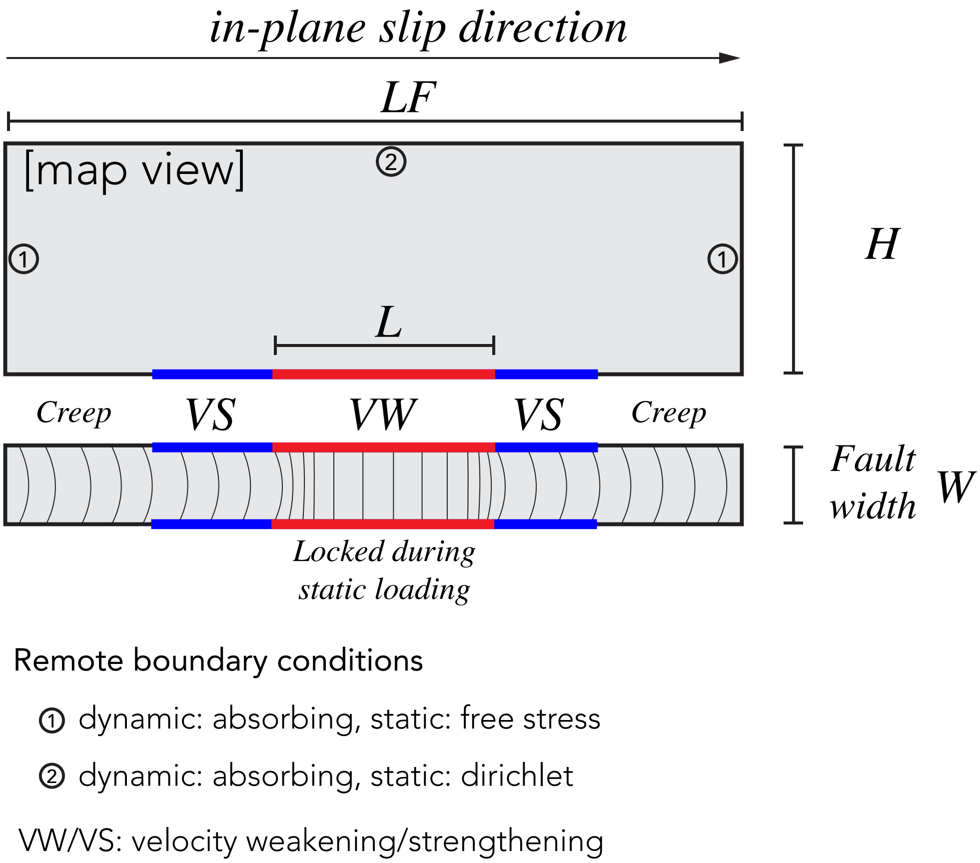

Figure S1. Schematics of model geometry and boundary conditions. We exploit the symmetry and only model half of the physical domain. The infinite domain truncated into a LF by H finite domain with a finite fault width W.

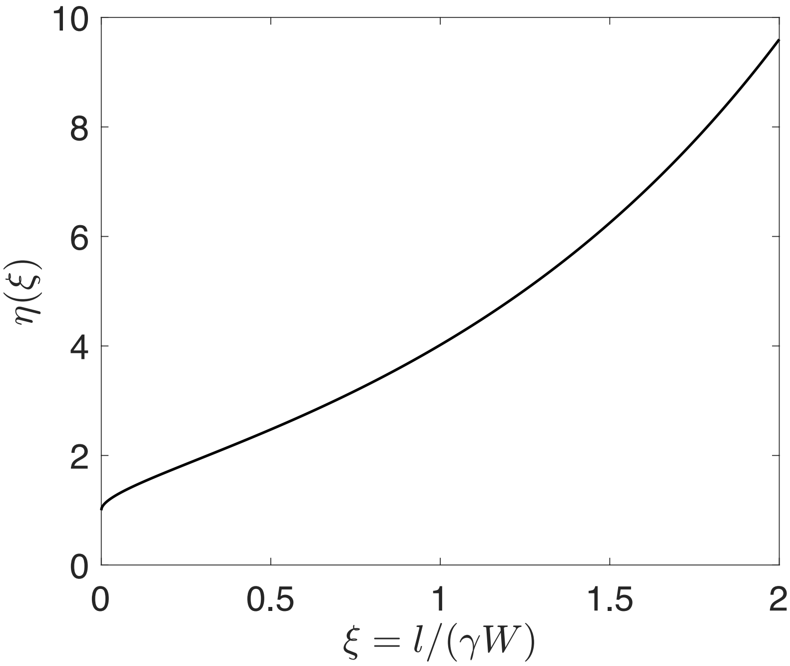

Figure S2. η as a function of $\xi = l/(\gamma W)$. η converges to 1 as ξ tends to 0 and diverges at large ξ.

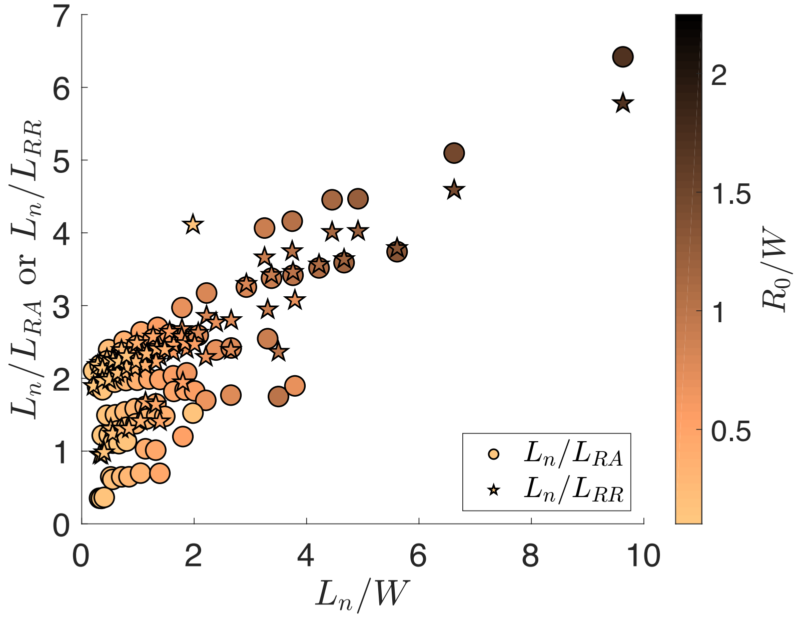

Figure S3. L_n/L_{RR} or L_n/L_{RA} as a function of L_n/W, colored by R_0/W. L_n is close to L_{RA} or L_{RR} only when both L_n/W and R_0/W are small.

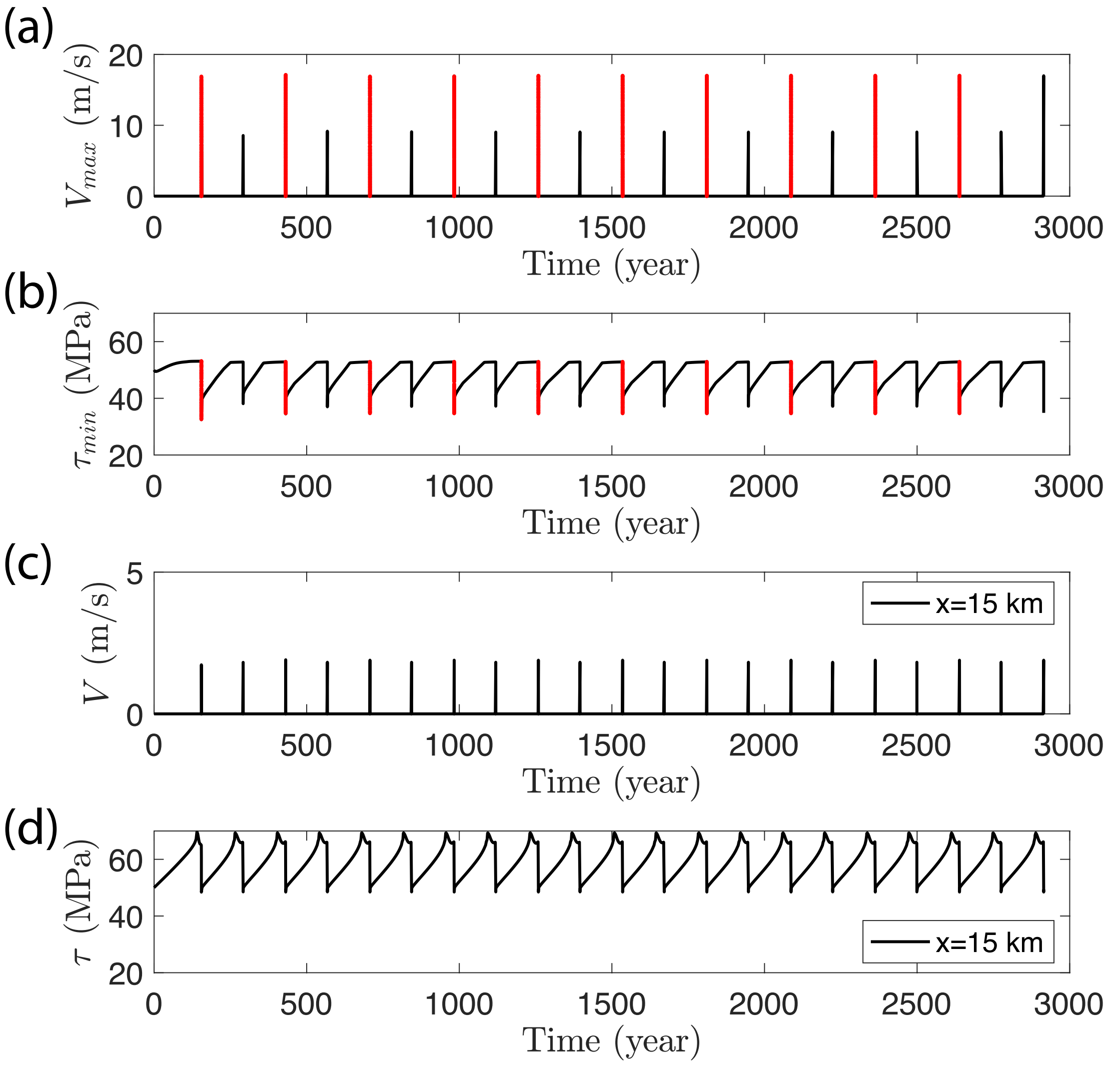

Figure S4. Time series of (a) maximum slip rate V_{max}, (b) minimum shear stress τ_{min} (c) slip rate and (d) shear stress in the middle of the nucleation patch at $x = 15$ km. Supershear events marked in red in (a) and (b). This simulation assumes $a/b = 0.2$ and $L_{RA}/W = 0.4$ and produces an alternation of supershear and sub-Rayleigh events. It is clear that supershear events have higher maximum slip rates and lower residual stresses. However, the shear stress and slip rate in the nucleation patch do not vary much across different events. The inter-event time is rather characteristic.

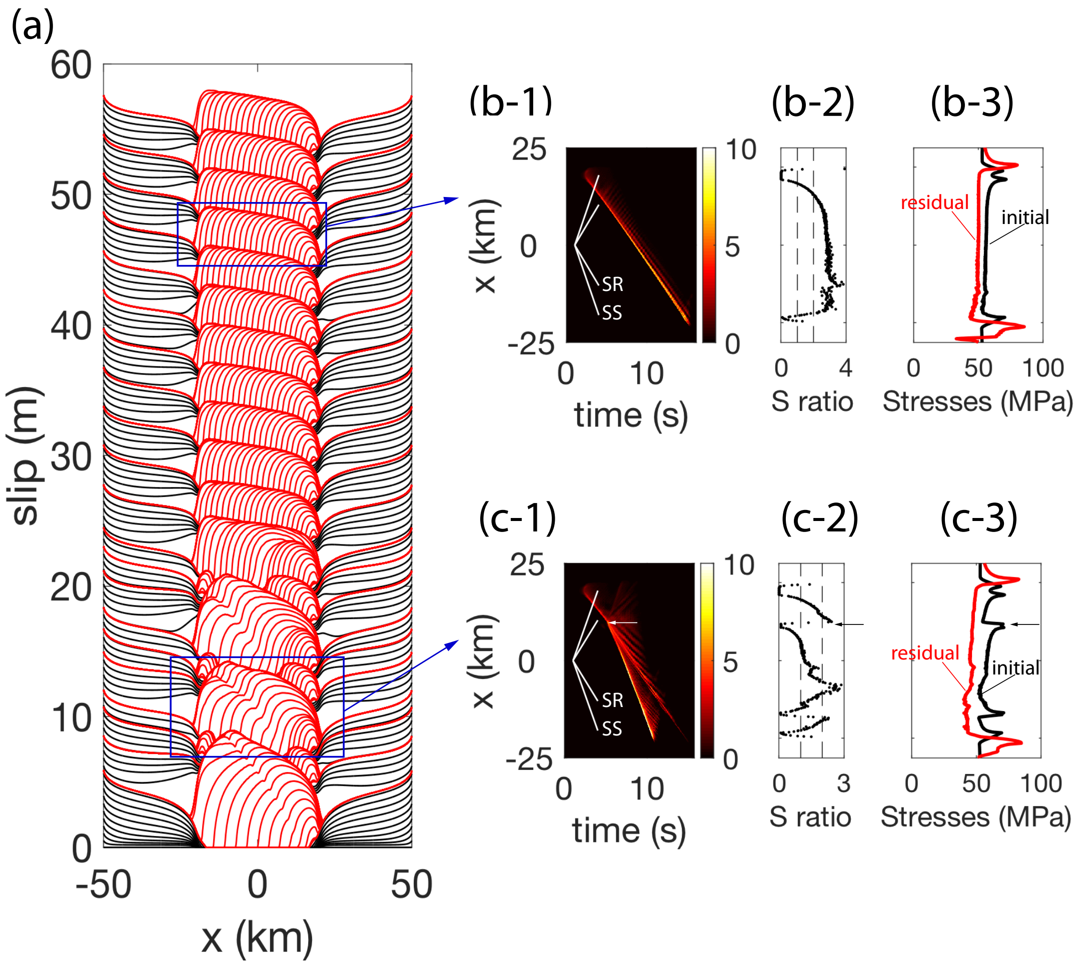

Figure S5. The accumulative slip for the entire sequence (a), space-time plot of slip rate (b-1,c-1), S ratio (b-2, c-2), initial and residual stresses (b-3,c-3) for marked events. The arrows in c-1, c-2, and c-3 highlight the coincidence between the position of the supershear (SS) transition and stress concentration from previous earthquakes. The sequence eventually stablizes to fully sub-Rayleigh (SR) earthquakes, such as event 18 shown in b-1, b-2, and b-3. However, two earthquakes (excluding the first one) manage to transition to supershear due to favorable stress heteogeneity.